








RESEARCH ARTICLE | AUGUST 09 2023

Lagrangian dynamics of particle transport in oral and nasal breathing **FREE**

Special Collection: [Flow and the Virus](#), [Flow and the Virus](#)

Hossein Seyedzadeh ; Wayne Oaks ; Jonathan Craig ; Mustafa Aksen ; Mario Sánchez Sanz ; Ali Khosronejad  



Physics of Fluids 35, 081903 (2023)

<https://doi.org/10.1063/5.0163658>

 CHORUS



Articles You May Be Interested In

On the Lagrangian dynamics of saliva particles during normal mouth breathing

Physics of Fluids (April 2022)

Numerical simulation of virus-laden aerosol transmission in real human respiratory airways

Physics of Fluids (October 2023)

A study of fluid dynamics and human physiology factors driving droplet dispersion from a human sneeze

Physics of Fluids (November 2020)



Physics of Fluids

Special Topics Open
for Submissions

[Learn More](#)

Lagrangian dynamics of particle transport in oral and nasal breathing

Cite as: Phys. Fluids **35**, 081903 (2023); doi: [10.1063/5.0163658](https://doi.org/10.1063/5.0163658)

Submitted: 18 June 2023 · Accepted: 27 July 2023 ·

Published Online: 9 August 2023



Hossein Seyedzadeh,¹ Wayne Oaks,¹ Jonathan Craig,¹ Mustafa Aksen,¹ Mario Sánchez Sanz,² and Ali Khosronejad^{1,a)}

AFFILIATIONS

¹Civil Engineering Department, Stony Brook University, Stony Brook, New York 11794, USA

²Department of Thermal and Fluids Engineering, Carlos III University of Madrid, Madrid 28911, Spain

Note: This paper is part of the special topic, Flow and the Virus.

^{a)} Author to whom correspondence should be addressed: ali.khosronejad@stonybrook.edu

ABSTRACT

We present a large-eddy simulation (LES) of saliva particle transport during normal human breathing through the nose and mouth. The flow of the air–saliva mixture is modeled using an Eulerian LES that is coupled with a Lagrangian particle tracking module to obtain trajectories of saliva particles in a room with stagnant air conditions. The coupled Eulerian–Lagrangian simulation yields novel insights into the intricate dynamics of Lagrangian coherent structures (LCS) and fundamental material lines that emerge from the saliva particles' trajectories during several breathing cycles. Further, we systematically compare the quantitative LCS diagnostics of mouth breathing with those of mouth and nose normal breathing. Analyzing the simulation results of human breathing from the mouth and nose, we show that, soon after the first breathing cycle, saliva particles form a series of roll-up vortex rings that propagate forward. The forward propagation of these vortex rings leads to the formation of an asymmetrical primary forefront vortex. The individual vortex rings continuously propagate forward, merging with the forefront vortex, and ascending along the limb of the leading vortex.

Published under an exclusive license by AIP Publishing. <https://doi.org/10.1063/5.0163658>

I. INTRODUCTION

With 766×10^6 confirmed cases and 6.9×10^6 deaths, the COVID-19 pandemic has heightened the importance of studying biological flow patterns and saliva particle transport.¹ The social distancing guidelines, recommended by the World Health Organization and the Center for Disease Control, at the onset of the pandemic were based on a dated science which did not include many factors in human breathing. Namely, the supposed dichotomy of big and small particles suffered arbitrary classification that did not consider the effects of the particle cloud's turbulence and speed or the effects of ambient temperature and humidity.² Consequently, it is crucial to conduct research on human respiratory events and the transportation of saliva particles to inform and standardize public health safety measures based on the latest scientific advancements.

At the onset of the pandemic, the guidelines on COVID-19 were not only inconsistent with each other but also based on dated experiments which did not fully capture the intricacies of particle transport from biological flows.^{3–5} These intricacies are broadly varied as there are many ways in which particle transport can manifest itself: in breathing, talking, coughing, and sneezing; for various physiological

factors including health, anatomy, sex, and age; and in settings with diverse degrees of particle size, temperature, and relative humidity.^{6–12}

In recent years, there has been a significant focus on conducting extensive experimental and computational studies to examine the human respiratory events' flow dynamic and their impact on the transport of aerosols. To complement the protection afforded by social distancing, face masks have been implemented in light of studies which supported their efficacy in curtailing saliva particles' spread in indoor settings.³ Hui *et al.*¹³ implemented laser visualization to test infection control measures with and without a face mask. There was a substantial decrease of dispersion distance in the cases with a face mask; however, there was substantial leakage at the interface between the mask and the nose. Upon tightening the mask, leakage was decreased. Dbouk and Drikakis¹⁴ observed a similar leakage at this interface in a coupled Eulerian–Lagrangian (EL) simulation of a mild cough, acknowledging that such leakage could considerably lower the mask's stated efficiency. Pendar and Pascoa¹⁵ advised that the social distance should be lengthened to 4 m for a sneeze as bigger droplets could not only travel farther but also contain higher viral loads. For this reason, they recommended reducing the contamination area by wearing a face mask and bending the head during a sneeze.

Using the outdated and simplistic models, more complex models have been developed to incorporate the complexities of human breathing, which included the nose's effect on particle transport and virus transmission.^{15–20} Mittal *et al.*¹⁹ incorporated the nose in their parameter for expulsion rate; though, the combination of mouth breathing, and nose breathing might not capture the nose's impact on particle transport and deposition. Zhou and Zou²⁰ recognized that the nose was crucial not only in the saliva particles' behavior upon exhalation but also in the saliva particles' deposition in the respiratory tract after conditioning and filtering of the breath. Liu *et al.*¹⁷ found that most particles were deposited within the first 30% of the nasal cavity's length. Specifically, most deposited particles fell around the cavity walls by the nasal valve.

Particle size is a substantial factor in saliva particles' transport and deposition. In a review of the experimentally tested dichotomy of particle size proposed by Wells,²¹ Bourouiba² suggested that the arbitrary dichotomy of big and small droplets did not reflect the reality of respiratory emissions. This finding was corroborated by Stiehl *et al.*²² by investigating saliva particles' emission from a sneeze through a combined experimental and numerical approach which utilized detached eddy simulation (DES). Mittal *et al.*⁴ highlighted that there is a critical size range from 50 to 150 μm over which the settling rate becomes greater than the evaporation rate. Through a Lagrangian particle tracking approach, Pendar and Páscoa¹⁵ noticed that as particle size increased, gravity and inertia gained a greater influence over the particles than aerodynamic drag and ambient flow field. In comparison, Renzi and Clarke²³ reported that particles of sizes 500 μm and greater could reach over 1.8 m for chosen ejection angles.

Evaporation should also be considered as it plays a major role in saliva particle transport and virus transmission. Zeng *et al.*¹¹ incorporated flow evaporation into the Navier–Stokes equations to study the impact of temperature and evaporation on saliva particles' settling and virus transmission. Li *et al.*¹⁰ modeled droplet dispersion for cases with varied degrees of evaporation and of proximity between human models. In all cases which they documented, evaporation significantly reduced the droplet count; however, it was noted that evaporated droplets could reach as far as unevaporated droplets and that evaporated droplets might have a higher viral concentration. Stiehl *et al.*²² reported that the maximum airborne time was much lower for desert relative humidity than for tropical relative humidity. Furthermore, the reduction of dehydrated solids for increased relative humidity implied a reduced risk of virus transmission in humid climates. Lieber *et al.*²⁴ conducted experimental research on saliva droplets to examine their evaporation behavior and how long they remain airborne. The objective was to better understand the airborne transmission of SARS-CoV-2.

If the effect of the nose breathing on the saliva particles' momentum should be considered, it might affect the saliva particles' trajectories, which could lead to a significant accumulation over the span of the breathing cycle.²⁵ Fontes *et al.*⁸ identified a jet redirection which resulted from the combined effect of the teeth and the nasal jets. They recorded a 300% increase in droplet content when the nasal cavity was blocked by congestion, and they observed that increased saliva viscosity decreased the transmission rate by 47% as droplet number decreased whereas droplet size increased. Islam *et al.*²⁶ developed a numerical model for particle transport with a focus on extra-thoracic airways. In their results, they measured a higher deposition rate in the nasal cavity and in the extra-thoracic airways in the case of nose breathing.

Studies such as Fontes *et al.*⁸ demonstrated that droplets expelled in mouth breathing follow the airflow's initial momentum, and the study of Behera *et al.*²⁷ highlighted the similarity between the cough jet's and the continuous free jet's temporal evolution; however, such studies did not consider the impact from the nose's two jets on airflow and aerosol dispersion. Through a hybrid Reynolds-averaged Navier–Stokes-large-eddy simulation (LES) turbulence method and a discrete phase model to visualize nasal airflow in sneezing, Salati *et al.*²⁸ observed that the left and right jets from the nostrils interfered and merged with each other after a given axial distance coinciding with a loss of initial momentum and a noticeable radial divergence. Also, Salati *et al.*²⁸ saw that nasal jets behaved likewise to turbulent free jets in parallel as remarked by Behera *et al.*²⁷ By employing direct numerical simulation with phase-averaging, Behera *et al.*²⁹ captured influential vortex structures: shear layer roll-up, jet-wake, and stack-wake. Their finding of the stack-wake's greater width, which results from a higher velocity than in the jet-wake, agrees with the findings of Salati *et al.*²⁸ In an experimental study with particle image velocimetry and planar laser-induced fluorescence, Zhang *et al.*³⁰ reported that influential vortex structures became denser at higher jet-to-crossflow velocity ratios, thereby leading to more intense mixing. In the same way as in mouth breathing, diverse physiological and environmental factors complicate nose breathing, and so such factors can be considered in studies on nose breathing. For instance, in a numerical study using the stress-blended eddy simulation (SBES), Bradshaw *et al.*³¹ observed that the nasal airway's geometry influenced respiratory particles' inspiration and expiration, and they underscored the onset of a pharyngeal jet from the trachea's anatomy.

Nasal jet flows and associated vortex structures add more complexity to respiratory particle dispersion, but the effects can be quantified to delineate coherent structures at play in particle transport. During normal breathing, there are periodic jet-like flows that expel saliva particles into the surrounding air, downwind from the individual. The highest speed of the air–saliva mixture during normal breathing typically falls between 0.5 and 1 m/s, which can generate a jet-like flow with $Re = uL/v$, where u and L , respectively, represent characteristic velocity and length and v denotes kinematic viscosity. The jet flow resulting from normal breathing comprises three-dimensional coherent vortical structures, which play a role in transporting saliva particles.²⁵ To track the saliva particles, one can couple a Eulerian flow solver with a Lagrangian tracking module to obtain the background air/saliva flow field and the trajectories of individual saliva particles.³² Haller³³ recognized stable and unstable manifolds or material surfaces, which constitute the Lagrangian coherent structures (LCS), and showed that these manifolds could impact particle transport by delineating two-dimensional invariant boundaries over which particle trajectories may not cross. LCS are common in natural systems as well as engineered systems, ranging from oceanic and atmospheric flows to aerodynamic and hydrodynamic flows.^{34–38}

In contrast to Eulerian diagnostic approaches such as the Okubo–Weiss criterion, the Q-criterion, and the Δ -criterion, LCS serve as a more reliable parameter of comparison between models as LCS do not depend on individual particle trajectories.^{35,39} The study of coherent Lagrangian patterns in the transportation of material particles can help to identify and understanding similar patterns of saliva particles' movement in normal breathing. The identification of LCS in biological fluid flows such as saliva particle transport could inform

expectations of particle transport behavior during human breathing, as well as public policies which restrict virus transmission.

Our objective is to understand the Lagrangian dynamics of saliva particle transport and the vortex patterns associated with human breathing through both the nose and mouth. Additionally, we aim to evaluate the impact of the interaction between the flow from the nose and mouth on the trajectories and transport of saliva particles. We conducted a high-resolution LES with the coupled Eulerian–Lagrangian approach to investigate the transport of saliva particles of various sizes during normal breathing from both the nose and mouth under indoor conditions. To illustrate the effect of simultaneous mouth and nose breathing, we compare the results of this study with a previously reported study in Oaks *et al.*³² in which particle trajectories were obtained for normal breathing through mouth only. The computational grids used in the simulations are fine enough to capture most of the relevant scales of motion. The range of saliva particle sizes considered in this work is from 0.1 to 10 μ m, which falls within the size range of aerosol particles produced during human breathing and is known to be large enough to carry viruses.^{1,2,40,41} Each size class of saliva particles is simulated as an active scalar, governed by the Boussinesq-type advection–diffusion equation, with a settling velocity that depends on the particle size.^{3,4,42–44} Saliva particles’ evaporation, which enhances particles’ travel distance significantly over multiple breathing cycles, is taken into account by gradually reducing the size and settling velocity of suspended particles.^{3,4} The three-dimensional geometry of the human body was incorporated into the model using the sharp interface curvilinear immersed boundary (CURVIB) method.^{43,45–51}

Our findings demonstrate that normal breathing through the nose and mouth generates distinct periodic trailing jets, leading circular vortex rings, and LCS which differ in dynamics and topology from those observed for mouth-only breathing in Ref. 32. These structures propagate forward and interact with the vortical flow patterns created during previous breathing cycles, albeit with altered dynamics. The intricate vorticity field can carry aerosols approximately two meters away from the source.

This paper is organized as follows. In Sec. II, we present the governing equations and boundary conditions of the coupled Eulerian and Lagrangian models. Subsequently, the computational details of this numerical study are presented in Sec. III. Then, we present the results of the study and discuss its findings in Sec. IV. Finally, we conclude this study in Sec. V.

II. GOVERNING EQUATIONS

A. Eulerian framework

The flow of air–saliva mixture is obtained by solving the incompressible and spatially filtered continuity and Navier–Stokes equations. These equations in non-orthogonal and generalized curvilinear coordinates, utilizing compact tensor notation (where i, j, l , and k range from 1 to 3), are expressed as follows:⁴⁵

$$J \frac{\partial U^j}{\partial \xi^j} = 0, \tag{1}$$

$$\frac{1}{J} \frac{\partial U^i}{\partial t} = \frac{\xi^i}{J} \left\{ -\frac{\partial(U^j u_i)}{\partial \xi^j} + \frac{1}{\rho_0} \left[\frac{\partial}{\partial \xi^j} \left(\mu \frac{g^{jk}}{J} \frac{\partial u_i}{\partial \xi^k} \right) - \frac{\partial}{\partial \xi^j} \left(\frac{\xi^j p}{J} \right) - \frac{\partial \tau_{ij}}{\partial \xi^j} + (\bar{p} - \rho_0) g \left(\frac{\delta_{i3}}{J} \right) \right] + f_i \right\}, \tag{2}$$

where u_i is the filtered l th Cartesian velocity component, $U^j = (\xi^j_l/J)u_i$ is the filtered contravariant volume flux, $\xi^i_l = \partial \xi^i / \partial x_j$ are the transformation metrics, $J = |\partial(\xi^1, \xi^2, \xi^3) / \partial(x_1, x_2, x_3)|$ is the Jacobian of the geometric transformation, $g^{jk} = \xi^j_l \xi^k_l$ are the components of the contravariant metric tensor, p is the filtered pressure, ρ_0 is the background density of the ambient air, \bar{p} is the density of the air–saliva mixture due to the breathing, μ is the dynamic viscosity, τ_{ij} is the sub-grid stress (SGS) tensor in the LES model, δ_{ij} is the Kronecker delta, and f_i is the body force due to the external effects, e.g., face mask effect, which we do not have here. The dynamic Smagorinsky model is employed to define the SGS terms of the LES, as follows:

$$\tau_{ij} - \frac{1}{3} \tau_{kk} \delta_{ij} = -2\mu_t \bar{S}_{ij}, \tag{3}$$

where \bar{S}_{ij} is the filtered strain-rate tensor ($=1/2(\partial u_i / \partial x_j + \partial u_j / \partial x_i)$). The eddy viscosity can be written with the following equation:

$$\mu_t = \rho C_s \Delta^2 |\bar{S}|, \tag{4}$$

where C_s is the Smagorinsky constant ($=0.09$); Δ is the filter size, i.e., the grid resolution; and $|\bar{S}| = \sqrt{2\bar{S}_{ij}\bar{S}_{ij}}$. Furthermore, the interaction between air and saliva within the mixture results in variations in air–saliva mixture’s density. These density fluctuations, which can be computed using the Boussinesq assumption, are expressed as follows:⁵²

$$\bar{p} = \rho_0(1 - \psi) + \rho_s \psi, \tag{5}$$

where ψ and ρ_s refer to the volume fraction and the density ($=1000 \text{ kg/m}^3$) of the saliva particles in the mixture, respectively. The saliva particles’ concentration is determined using the following convection–diffusion equation:⁵²

$$\frac{1}{J} \frac{\partial(\rho_0 \psi)}{\partial t} = \frac{\partial}{\partial \xi^j} \left[(\mu \sigma_L + \mu_t \sigma_T) \frac{g^{jk}}{J} \frac{\partial \psi}{\partial \xi^k} \right] - \frac{\partial}{\partial \xi^j} \left[\rho_0 \psi (U^j - W^j \delta_{i3}) \right], \tag{6}$$

where $W^j = (\xi^j_3/J)w_s$ refers to the contravariant volume flux of saliva concentration in the vertical direction due to the settling velocity (w_s) of the particles, μ_t is the eddy viscosity, and σ_L and σ_T are the laminar and the turbulent Schmidt numbers, considered to be 100 and 0.75, respectively (for more details, see Ref. 53). The settling velocity of the particles is determined as³²

$$w_s = \frac{D_p^2(\rho_s - \rho_0)}{18 \mu}, \tag{7}$$

where D_p is the diameter of the saliva particle.

B. Lagrangian framework

A one-way Eulerian (LES) and Lagrangian simulation of saliva particle transport is performed, in which we first solve for the background Eulerian velocity field using the LES model. In the Eulerian computations, the saliva particles’ evaporation and its impact on the saliva plume’s concentrations are neglected. While the continuum concentration field of the air–saliva mixture is obtained, the stratification effect of the air–saliva mixture flow is taken into the Eulerian equations of motion via Boussinesq approximation. Once the so-obtained

background velocity field is obtained, it is utilized to track the trajectories of discrete individual saliva particles in a one-way manner (i.e., the dynamics of the discrete saliva particles is impacted by the background Eulerian flow, but the background flow field is not influenced by the discrete saliva particles). For each saliva particle, we solve the following Lagrangian particle tracking equations to obtain its trajectory:³²

$$\frac{\partial x_p}{\partial t} = u_p, \tag{8}$$

$$m_p \frac{\partial u_p}{\partial t} = f_g + f_D, \tag{9}$$

where x_p , u_p , and m_p are the saliva particle's position, velocity, and mass, respectively. Additionally, f_g and f_D are the gravity and drag forces, respectively. Since the air-saliva mixture contains relatively small saliva particles, the forces such as lift, added mass, collision, and forces due to fluid stresses are not considered.³² Thus, the forces considered in the Lagrangian particle tracking method are as follows:

$$f_g = \left(1 - \frac{\rho_s}{\rho_0}\right) m_p g, \tag{10}$$

$$f_D = -\frac{1}{2} \rho_0 C_d \frac{\pi D_p^2}{4} \|(u_f - u_p)\| (u_f - u_p), \tag{11}$$

where C_d is the drag coefficient and u_f is the fluid (background Eulerian) velocity. The drag coefficient is obtained as⁵⁴

$$C_d = \begin{cases} \frac{24}{Re_p}, & Re_p < 0.1, \\ 3.69 + \frac{22.73}{Re_p} + \frac{0.0903}{Re_p^2}, & 0.1 < Re_p < 1, \\ 1.222 + \frac{1.667}{Re_p} - \frac{3.889}{Re_p^2}, & 1 < Re_p < 10, \end{cases} \tag{12}$$

where $Re_p = \rho_0 D_p \|(u_f - u_p)\| / \mu$ is the saliva particle's Reynolds number. Given the particle sizes and the flow velocity described in Sec. III, Re_p is consistently smaller than 10. A validation study of the Lagrangian tracking model is presented in the Appendix.

C. Boundary conditions

A periodic boundary condition was employed in the spanwise direction. A no-slip boundary condition was applied on the human anatomy and the ground. For the top and outlet boundaries, Neumann outflow condition was enforced. The inlet velocity of the normal breathing was calculated as follows:^{25,32}

$$u = \frac{V_t}{T_b A} \pi \cos\left(\frac{2\pi t}{T_b} + \frac{\pi}{2}\right), \tag{13}$$

where V_t is the tidal volume of breathing ($1 \times 10^{-3} \text{ m}^3$), T_b is the period of breathing ($=5 \text{ s}$), t is the instantaneous time, and A is the area of the outlet opening.³² This relation obtains a maximum velocity of nearly 0.9 m/s. Considering 75% of the tidal volume to occur through the mouth, and 25% of it takes place through the nose, we prescribed a horizontal velocity component of $0.75 u$ at the mouth, while setting the exit velocity of the air-saliva mixture from the nose to have a magnitude of $0.25 u$.

III. COMPUTATIONAL DETAILS

To represent the human anatomy accurately in our simulations, we utilized the sharp interface CURVIB^{3,25} method with wall model reconstruction.^{43,50,51} The open-source software of Blender was used to generate the human geometry, which was discretized using an unstructured grid system [see Fig. 1(c)]. The constructed human geometry was 1.82 m high, and its mouth was located 1.67 m above the ground. The bottom of the nose is located 0.033 m higher than the mouth. The nose is inclined with an angle of 18.6° with respect to vertical direction (along the z-axis). The mouth opening is characterized

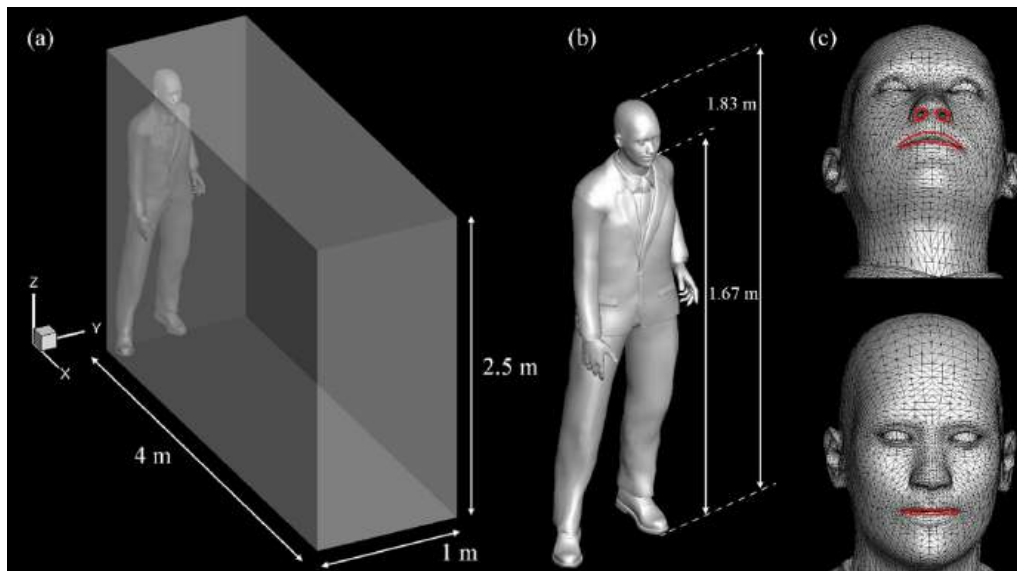


FIG. 1. Schematic of simulation domain (a), human anatomy (b), and the opening of the nose and mouth (c).

22 November 2024 06:38:20

by a curved elliptical shape, which is ~ 0.0351 m wide and 0.01 m high. The nose opening consists of two ellipses, each with a typical nostril width of 0.009 m. The major and minor axes of the two nose-opening ellipses are 0.0045 and 0.004265 m. We note that the minor axis of the nose is inclined with the nose angle in relation to the z-direction. This geometry permits a realistic representation of the nose to investigate the impact of different fluid-dynamic factors on human normal breathing.

The computational domain encompasses a room with dimensions of 4.0 m in length, 1.0 m in width, and 2.5 m in height [Fig. 1(a)]. The human model is positioned on the left side of the room. A structured Cartesian grid was employed to discretize the domain. The Cartesian grid is stretched with a ratio of 1.002 in all directions from the mouth. This stretching allows for a fine resolution of 0.5 mm in the vicinity of the nose and mouth. The so-obtained computational grid consists of over 650×10^6 grid nodes, with grid spacing ranging from 0.5 mm near the face to approximately 2 mm at a distance of 4 m away from the face. The Lagrangian particle tracking was conducted for 110 000 saliva particles released at the nose and mouth openings into the room.

An empirical approach reported in Ref. 55 was adopted to consider the evaporation's impact on the saliva particles' transport. This approach describes a rapid reduction in particle size due to evaporation (see Fig. 2), which, in turn, modifies the settling velocity and drag force of individual particles.

As seen in Fig. 2, the non-linear time variation of $(D_p/D_0)^2$ is coded to describe the particle evaporation. In this figure, the particle diameter, D_p , is normalized with initial particle diameter, $D_0 = 10 \mu\text{m}$. Based on Ref. 56, larger droplets, exceeding $5 \mu\text{m}$, generally remain trapped in the upper respiratory tract, specifically the oropharynx (nose and throat areas). Thus, one assumed that the saliva particles released from the nose and mouth are of the similar size range. Furthermore, we assume that soon after saliva particles are exhaled, their sizes stabilize at $0.1 \mu\text{m}$ and remain constant thereafter. This stabilization occurs after approximately 0.2 s after particles are exhaled and the time associated with that is denoted as $T_0 = 0.2$ s. We should also mention that once the water content evaporates from a saliva

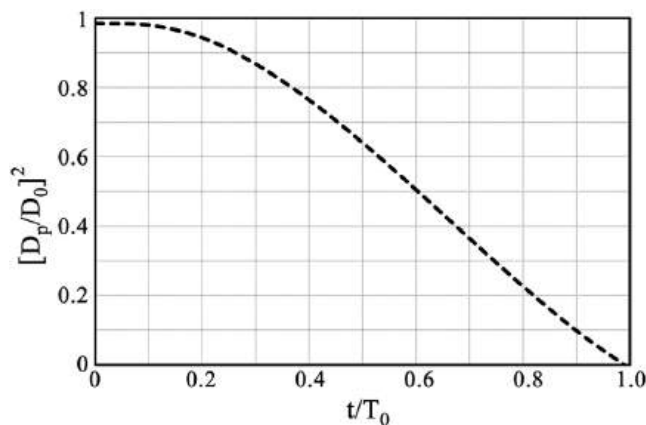


FIG. 2. Time variation of the square of normalized saliva particles diameter to prescribe the effect of evaporation on particles.⁵⁵ At $t/T_0 > 1$, the ratio $(D_p/D_0)^2$ converges to 10^{-4} and stays constant thereafter.

droplet, it attains a stable final size that remains unchanged for several hours. Analyzing numerous droplets of different sizes, researchers noted a consistent pattern: the final droplet diameter consistently corresponds to roughly 20% of the initial diameter. Importantly, this correlation remains constant irrespective of the ambient conditions, encompassing temperatures ranging from 20°C to 29°C . The presence of salts and proteins within saliva droplets accounts for this phenomenon.²⁴

At the diameter of $0.1 \mu\text{m}$, the settling velocity of the saliva particles is nearly $0.3 \mu\text{m/s}$, i.e., they can stay suspended in stagnant ambient air condition stagnant indoor air for days before they settle down on the ground. The insignificance of the gravitational forces in comparison to the viscous forces on the suspended particle can be examined using the Galileo number of the saliva particles, as well.³² The Galileo number of the saliva particles is in the order of $O(10^{-4})$ which is greatly smaller than one. Furthermore, to show that the studied saliva particles strictly follow the streamlines of the breathing flow, we calculate the Stokes number of the saliva particles that is a function of the characterization length and velocity. For the present breathing flow from the mouth and nose, the Stokes number is in the order of $O(10^{-6})$. And, since the Stokes number is greatly smaller than one, it can be said that the response time of the largest saliva particles is faster than the smallest timescale of the breathing flow. In other words, one can say that the saliva particles very well follow the streamlines of the breathing flow.

Finally, the simulation was carried out using 320 processors on a Linux cluster with 1216 Intel Xeon 3.3 GHz cores for nearly seven months of clock time. To reduce the computational cost of these simulations, the following simplifying assumptions are made: (a) the face and anatomy of the person is assumed to remain stationary throughout the breathing process; (b) stagnant air is considered the initial conditions for the airflow in the room; (c) the influence of thermal stratification around the body is neglected; (d) the condensation of exhaled saliva particles is not considered; (e) the density of exhaled particles is assumed to remain constant during the breathing process; (f) the saliva particles released from the nose and mouth are of the same size range; (g) the saliva particles are assumed to evaporate and reach a stable diameter of $0.1 \mu\text{m}$; (h) only a mouth-to-nose breathing ratio of 75%–25% are considered, assuming that most of the tidal volume is exhaled through the mouth; (i) the nose flow occurs at an angle of 18.6° ; and (j) an identical nasal airway's geometry is considered for both of the two nose openings. We recognize that further investigations are required to study the normal breathing with other mouth-to-nose breathing ratios and nose angles.

IV. RESULTS AND DISCUSSION

A. Saliva particle transport at initial stage of normal breathing

In this study, one breathing cycle takes 5 s which includes a 2.5-s exhale phase and 2.5-s inhale phase. Soon after exhaled, saliva particles undergo rapid evaporation reaching their terminal size of $0.1 \mu\text{m}$. Thus, saliva particles in the room have a broad spectrum of sizes, ranging from 0.1 to $10 \mu\text{m}$ in diameter. As described in this section, the expelled mixture of air and saliva during normal breathing forms a longitudinal flow resembling a jet, accompanied by a prominent vortex ring at its forefront.²⁵

Figure 3 depicts the evolution of vortical structures identified by the saliva particles' trajectory during the initial stages of normal breathing through both the nose and mouth.

Also, for the sake of comparison, we plot in Fig. 4 the particle trajectories for normal breathing through mouth only, as reported by Oaks *et al.*³² As seen in Fig. 3, the saliva particles cloud is generated and expands radially from both the nose and mouth. At the beginning of the first breathing cycle, the particle cloud is unaffected by the nose flow and behaves similar to the flow from the mouth only [Figs. 3(a) and 4(a)]. Immediately afterward, however, the particles in the starting jet's shear layer roll up and form a vortex ring [Figs. 3(b) and 4(b)]. At this stage, which is after about 1 s from the start of the first exhale, due to the effect of flow from the nose, the mouth jet bends downward accumulating particles on the lower side of the shear layer. This is when the particle trajectory of the mouth and nose breathing starts to deviate from that of mouth-only breathing [Figs. 3(b) and 4(b)].

When the first inhalation phase starts, i.e., after 2.5 s, the vortex ring undergoes the pinch-off process completing the formation of the vortex ring. This process occurs when the translational velocity of the starting jet aligns with that of the vortex ring.⁵⁷ As described by Oaks *et al.*,³² in the case of mouth breathing, the pinch-off process is

accompanied by the formation of two trailing jets [Fig. 4(c)]. In the case of mouth and nose breathing, as seen in Fig. 3(c), similar trailing jets are also present; however, they are asymmetric. The observed asymmetry is caused by the impact of the cross flow from the nose. As time goes on, the vortex ring from the present simulation continues to move forward while gradually losing momentum [Fig. 3(d)]. Unlike the vortex ring of mouth breathing in Fig. 4(d), the vortex ring and the trailing jet in the present simulation are far from symmetrical. As the breathing process continues and with each new breathing cycle, particles in the plume gain momentum and transfer it to the preceding particles which induces a radial expansion of the previous vortex ring. As discussed in Secs. IV B and IV C of this paper, eventually, these particles become a part of the front of the particle plume. The newly formed vortex rings move forward and capture the vortex front, carried outward along the leading vortex's material line. In all of these developments, the cross flow from the nose forces the particle plume to become tilted heavily downward. In other words, the jet flow from the mouth exhibits a bending motion in the direction of the cross flow and expands in width as it progresses downstream, which is consistent with the findings of Mahesh.⁵⁸

The phenomenon known as jet in crossflow (JICF) is commonly observed in nature, such as in volcanoes, and is also widely utilized in

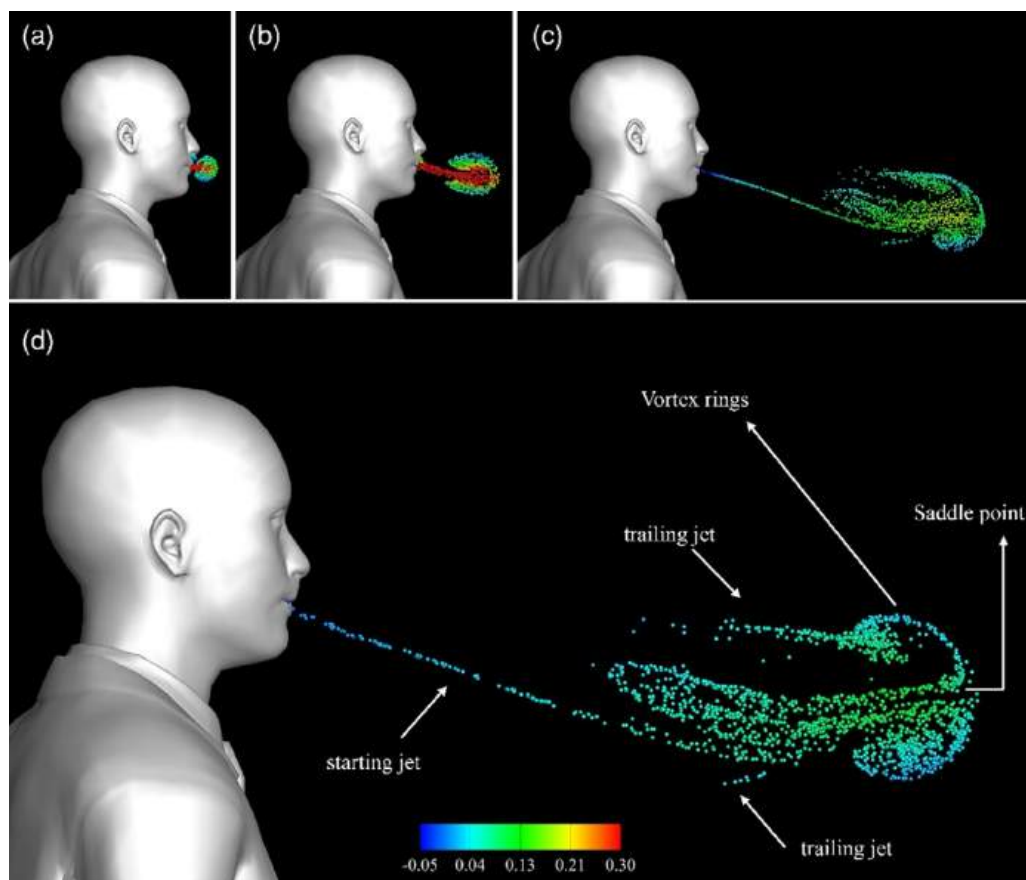


FIG. 3. The development of coherent flow structures during the first efflux of the nose and mouth breathing. These panels show (a) initial particle expansion at $t = 0.5$ s, (b) formation of the first vortex ring at $t = 1$ s, (c) formation of vortex head and trailing jets at $t = 3.25$ s, and (d) the coherent flow structures at $t = 5.0$ s. Particles are colored with their streamwise velocity (m/s). Panels show saliva particles on a 5-cm-thick layer around the sagittal plane during the normal breathing from the nose and mouth.

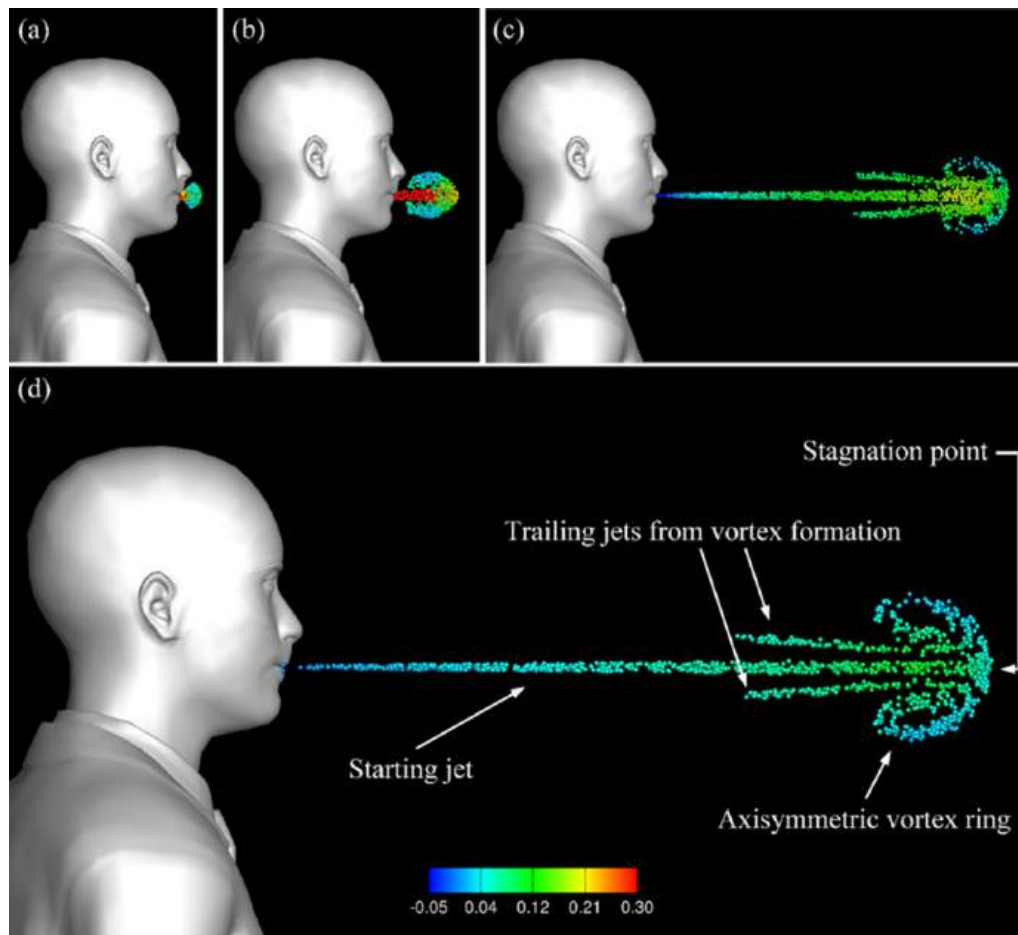


FIG. 4. The development of coherent flow structures during the first efflux of mouth breathing.²⁶ These panels show (a) initial particle expansion at $t=0.45$ s, (b) formation of the first vortex ring at $t=0.85$ s, (c) formation of vortex head and trailing jets at $t=3.3$ s, and (d) the coherent flow structures at $t=5.0$ s. Particles are colored with their streamwise velocity (in m/s). Panels show saliva particles on a 5-cm-thick layer around the sagittal plane during the normal breathing from the mouth.

industrial settings, like dilution jets and film cooling in gas turbines. In simple terms, JICF refers to the interaction that takes place when a jet exits an orifice and interacts with the mainstream fluid flowing across the orifice's vicinity.³⁰ As mentioned, the flow emitted from the nose interacts with the flow from the mouth, resembling the characteristics of transverse jets. Such transverse jets are a commonly observed phenomenon in the nature and engineering applications. For instance, the plume emitted from the Kirishima volcano in Japan⁵⁸ or the fuel injection in gas turbine engines⁵⁹ constitutes just two of such examples. Past studies have attempted to investigate the intricate behaviors of transverse jets. For example, Kelso *et al.*⁶⁰ conducted a series of experiments to classify the flow characteristics of cross flows based on their Reynolds numbers. Cortelezzi and Karagozian⁶¹ investigated the formation and evolution of vortex rings leading to counter-rotating vortices (CRV). CRVs represent swirling flow patterns that are induced by the interaction of cross flows and jets. Moreover, Cortelezzi and Karagozian⁶¹ illustrated that cross flow and jet interactions exhibit remarkable complexity, manifesting various distinct patterns such as folding, roll-up, and tilting.

They indicated that the counter-rotating vortex pairs (CRVPs) are the primary fluid characteristic associated with transverse jets. As reported by Fric and Roshko,⁶² the proximity of the jet exhibits four distinct coherent structures arising from the three-dimensional interaction between the jet and crossflow. These coherent structures include (1) the counter-rotating vortex pair (CRVP), (2) shear layer vortices, (3) wake vortices, and (4) horseshoe vortices. In this study, we have observed two of these structures: the jet shear layer vortices and counter-rotating vortex pairs. The jet shear layer vortices are manifested due to the Kelvin–Helmholtz instability of the annular shear layer that separates from the edge of the nose, predominantly influencing the initial portion of the nose jet. On the other hand, the vortex pair emerges because of the nose jet's impulse on the crossflow from the mouth. Initially, it forms in the near field, where the flow is pressure-driven, and gradually becomes dominant in the far field, characterized by the momentum-driven flow.

We plot in Fig. 5 the CRVPs of the normal breathing from the mouth and nose at $t=2.5$ s. The locations in front of the person where these CRVPs are visualized are marked with red lines in Fig. 5(a).

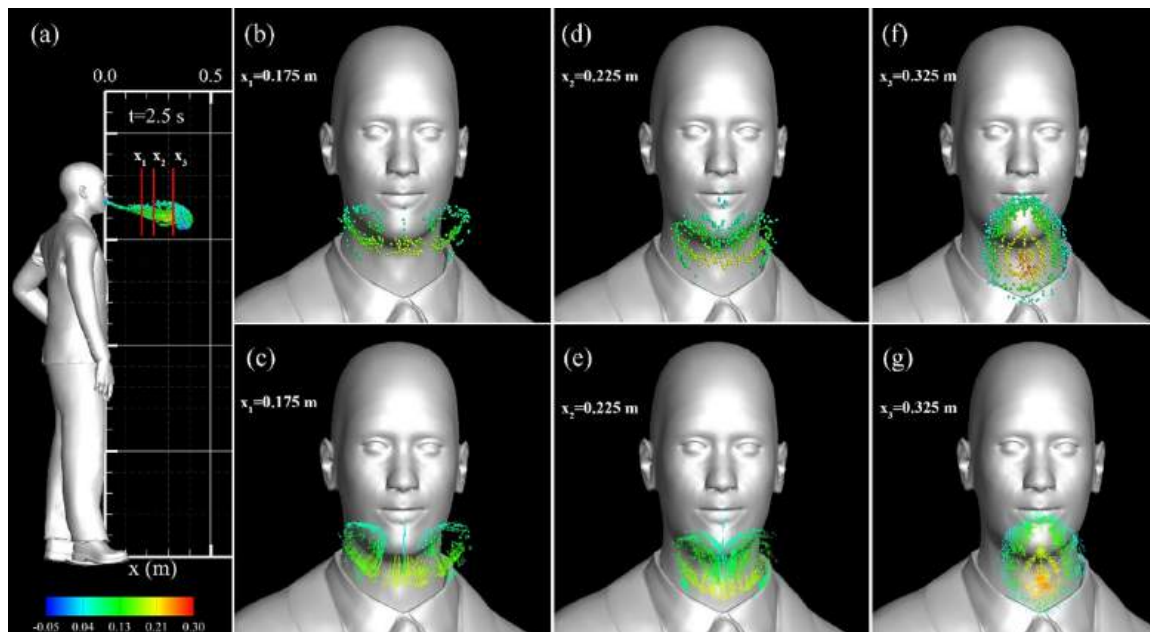


FIG. 5. Front view of simulated snapshots of normal breathing from nose and mouth at the first breathing cycle on various planes in the streamwise. Locations where the front views are taken are marked with the three red lines in (a). Each red line marks the middle of a 5-mm-thick plane. (b) and (c), (d) and (e), and (f) and (g) views are taken from the first, second, and third red lines in (a), respectively. (b), (d), and (f) show the computed particles, while (c), (e), and (g) show their corresponding particle vector field. Particles and vectors are colored with their streamwise velocity in m/s.

As seen in Figs. 5(b)–5(g), the cross section of the jet emitting from the mouth near the person evolves from its circular shape to form a pair of counter-rotating vortex. The flow behavior near the person can be explained by the presence of an adverse pressure gradient caused by the cross flow from the nose. This adverse pressure gradient results in the formation of a high-pressure region over the jet flow emitted from the mouth. And, subsequently, the jet flow from the mouth undergoes a deceleration process, leading to a velocity profile that is skewed downward. As a result, the jet's shear layer becomes asymmetrical deviating from a shear layer under the constant pressure gradient conditions. This asymmetry gives rise to the formation of the pair of CRV coherent vortex structures, as seen in Fig. 5. As the fluid particles move into the stagnant air, the counter-rotating vortex pairs begin to converge. In other words, as distance from the mouth increases, the two counter-rotating vortices approach each other and eventually come into contact, causing the counter-rotating vortex pairs to dissipate (Fig. 5). Also, the collision of the vortex pair leads to the disappearance of the lateral (spanwise) velocity component of the single vortex ring with an elevated streamwise velocity component near the lower portion of the vortex. The relatively higher streamwise velocity in the lower portion of the plume is what contributed to the roll-up of the plume at later times. If most of the flow is from the nose, say 90% from nose and 10% from the mouth, we speculate that the transverse jet structure would be modulated, owing to the fact that the mouth flow would act as the cross flow, while the nose flow would constitute the primary jet flow. It also can be speculated that—in the case of dominant nose breathing—the breathing direction would align with the nostrils. Because of the nature of the coherent structures arising from transverse jets, it can be speculated that when most of the

tidal volume originates from the nose, the breathing plume would primarily manifest a dominant vortex ring and, like the mouth dominant breathing case, eventually break down into smaller vortex rings.

B. Saliva transport at later stages of normal breathing

The analysis of saliva particle trajectories allows us to identify the elements that form LCS, including vortex rings and their accompanying trailing structures. During each cycle of normal breathing, the exhaled particles constitute a vortex ring which is accompanied by its trailing structures. The first vortex ring, referred to as the vortex front, imparts velocity to the subsequent rings, thereby accelerating their movement. As subsequent breathing cycles occur and advance forward, they entrain the vortex front and progress to the lateral expansion of the vortex front.

In Figs. 6(a) and 7(a), we plot the simulations results of the saliva particle transport during normal breathing through both the mouth and nose at different times after the start of the breathing cycles from the sagittal and top views, respectively. For comparison, we plot in Figs. 6(b) and 7(b) the corresponding results for the breathing from the mouth only. As seen, the air–saliva plume propagation is based on the accumulation of momentum over time, which is consistent to the findings reported by Khosronejad *et al.*²⁵ As seen in Fig. 6(a), the effect of the cross flow from the nose is evident in the bending of the mouth jet-like flow toward. Additionally, each vortex ring undergoes a rolling-up process facilitated by the presence of a high-velocity region in the lower section of the vortex ring. This is a significant contrast to the topology of the particle plume associated with the mouth-only breathing in Fig. 6(b) that has a rather straight jet with a slightly tilted

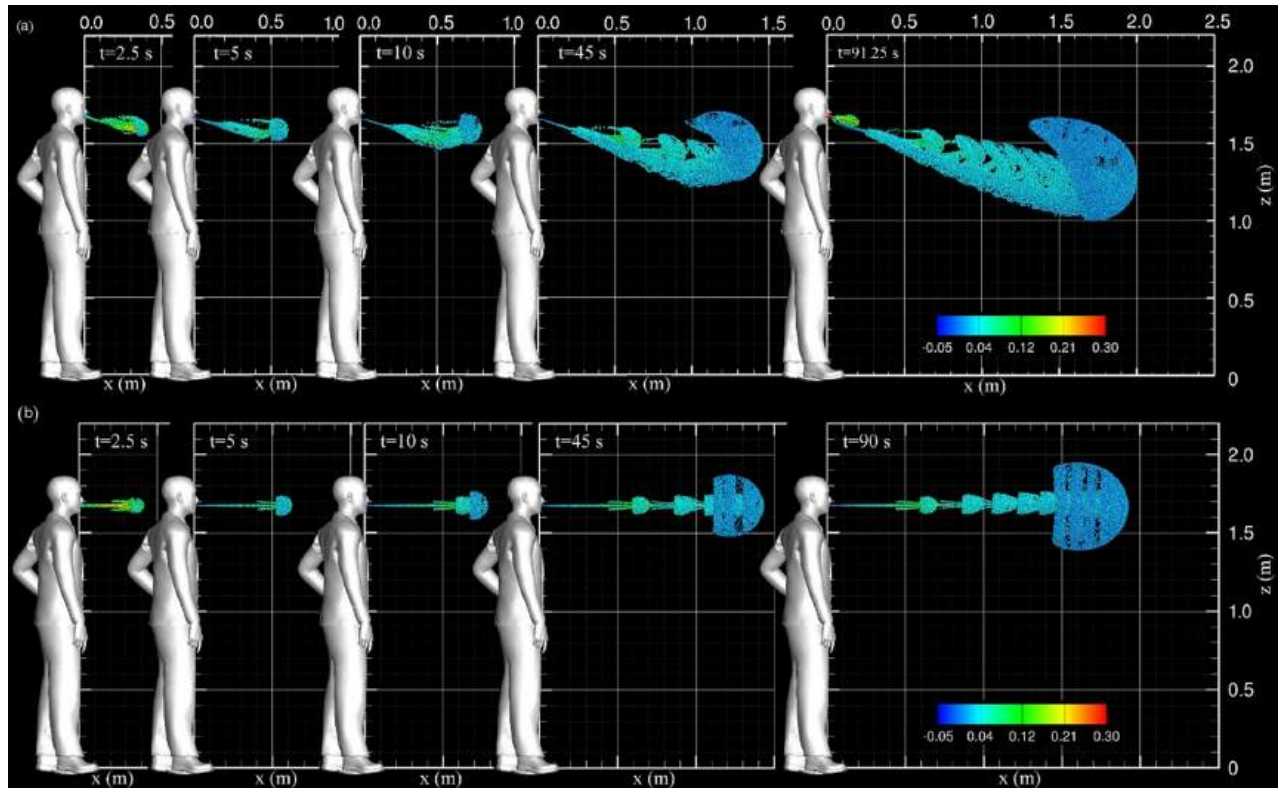


FIG. 6. Simulated snapshots of saliva particles transport during normal breathing: (a) from nose and mouth simultaneously and (b) from the mouth only.²⁶ The results are shown on the sagittal plane view. Saliva particles are colored with their streamwise velocity in m/s.

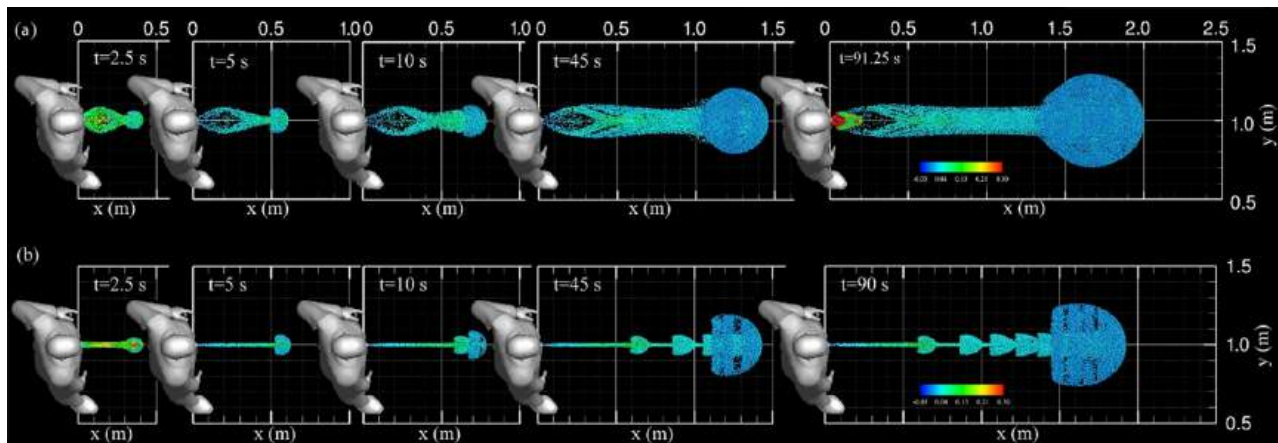


FIG. 7. Simulated snapshots of saliva particles during normal breathing: (a) from the nose and mouth simultaneously and (b) from the mouth only²⁶ from the top view. Particles are colored with their streamwise velocity in m/s.

(due to the gravitational effect) circular vortex ring at its forefront.³² Also, Fig. 7(a) provides further insight into the impact of the cross flow on the mouth jet that appears to result in the thickening of the jet flow from the mouth. As seen, the jet flow from the mouth exhibits a bending motion in the direction of the cross flow from the nose

and expands in the spanwise direction, i.e., widening the plume, as it progresses downstream. This finding is consistent with those of Mahesh⁵⁸ for the widening of the jet flows in the presence of the cross flow. A comparison of the present results [Fig. 7(a)] with those of the breathing through the mouth only [Fig. 7(b)], once again

shows the stark impact of the nose flow on the widening of the plume and modulation of the forefront vortex ring. It should be mentioned that, in the present study, the simulation was continued for about 91 s, at which the forefront of the saliva plume was observed to still propagate forward, albeit at a gradually decreasing speed, due to the ongoing and periodic exhalation process. As seen in Figs. 6(a) and 7(a), at this time, the saliva plume has reached 2 m from the person passing the Center for Disease Control's social distancing guideline of 1.8 m.⁶³ The simulation of the normal breathing through the mouth only was continued for over 91 s and the saliva plume reached 2 m after ~ 100 s.³²

Furthermore, Fig. 8 illustrates a comparison of saliva particle transport through both the nose and mouth to that of the mouth only by a Poincare map-like depiction, which shows the trajectories of saliva particles in a 5-cm-thick plane over the sagittal plane. These visualizations highlight the presence of a fractal-like LCS composed of vortex rings and their associated trailing structures in both breathing cases, which are created through the rapid expansion of an unstable shear layer. However, the influence of the flow from the nose on the mouth jet-like flow causes the plume to bend leading to the formation of fractal-like coherent structures in the upper region of the air-saliva plume. This effect leads to the rolling up of the vortex ring, generating an asymmetric vortex front [Fig. 8(a)]. In other words, unlike the case of mouth-only breathing which generated a relatively symmetrical and

straight plume with a forefront circular vortex containing an upper and a lower limb [Fig. 8(b)],³² breathing through both the mouth and nose generates an asymmetrical bended plume with a forefront vortex ring with a single upper limb [Fig. 8(a)].

Examining the simulation results of the LCS in mouth-only breathing and mouth-and-nose breathing, as seen in Figs. 6–8, we argue that there is some sort of time-periodic solution for the mouth-only breathing, while the periodic-solution is less obvious in our results of the mouth-and-nose breathing. Per its definition, a time-periodic solution can be identified as a solution in which there is a positive real number Γ such that $\kappa(t + \Gamma) = \kappa(t)$, where $\kappa(t)$ and $\kappa(t + \Gamma)$ represent particle trajectories at time t and $t + \Gamma$, respectively.⁶⁴ As seen in Figs. 6–8, in the case of the mouth-only breathing, the simulation results eventually reach a mild time-periodic solution in which the newly exhaled particles would join the primary vortex repeating a similar pattern of particle movement. This is mainly due to the presence of a single jet flow effluxing from the mouth and propagating forward horizontally. On the other hand, in the mouth-and-nose breathing case of Figs. 6–8, a time-periodic solution seems less obvious. It can be readily seen that the plume of saliva particles in the case of the mouth-and-nose breathing is constantly evolving and deforming throughout the breathing process. This less periodic solution seems to be a direct result of the cross flow from the nose, which constantly bends the body of plume downward.

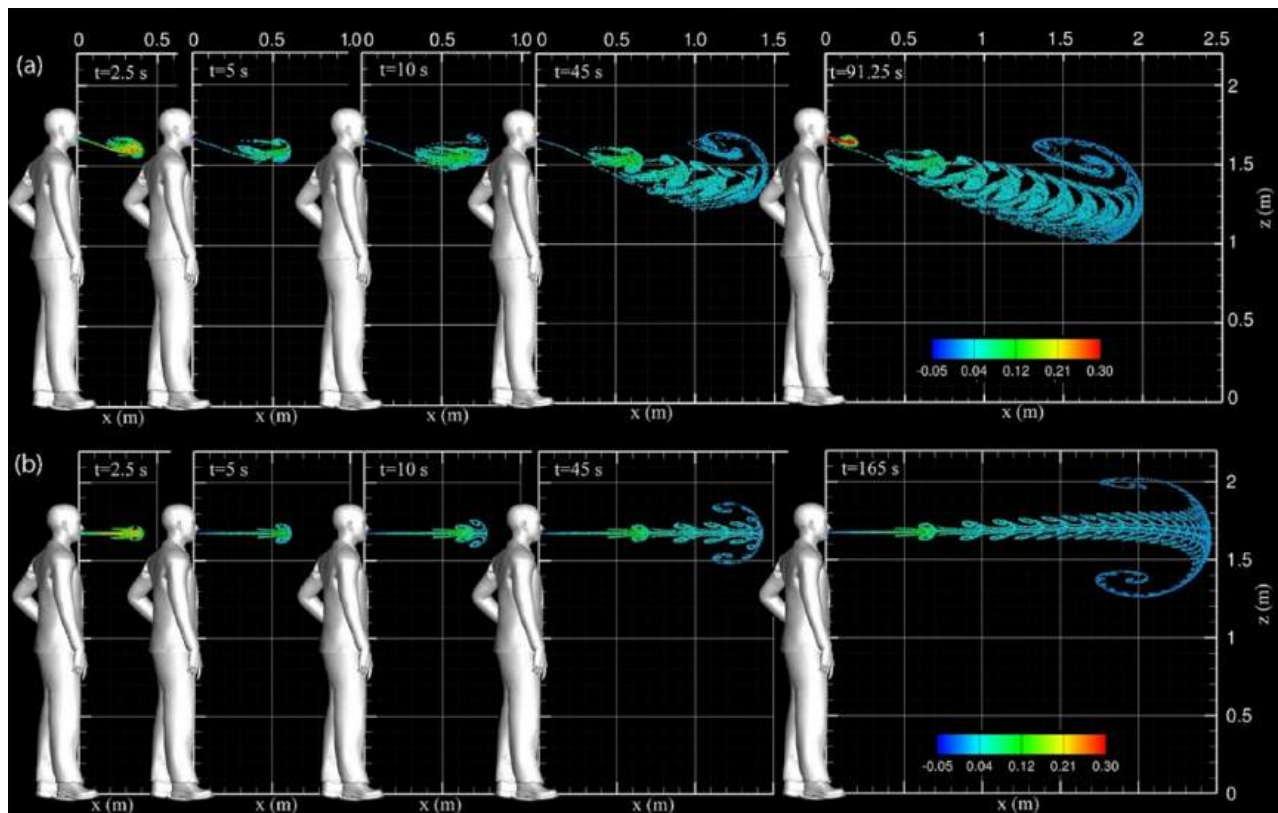


FIG. 8. Simulated snapshots of saliva particles on a 5-cm-thick layer around the sagittal plane during normal breathing: (a) from the nose and mouth simultaneously and (b) from the mouth only.²⁶ Particles are colored with the streamwise velocity in m/s.

C. LCS diagnostic of saliva particle transport at later stages of normal breathing

LCS of saliva particles can be utilized to describe the vortical flow structures and dynamic characteristics of the unsteady flow field of normal breathing. To do so, we analyze the LCS generated by the coupled Eulerian–Lagrangian simulation of normal breathing through the nose and mouth. LCS represent specific material surfaces that organize the flow and play a significant role in Lagrangian particle dynamics. According to Haller,³⁹ there are various approaches to obtain material lines and visualize the LCS. Among those are the Finite Time Lyapunov Exponents³⁵ which has been previously employed by Oaks *et al.*³² in the context of normal breathing through the mouth.

Herein, we adopt first Haller’s approach (Ref. 35) to identify the key material lines in the air–saliva mixture of normal breathing through the nose and mouth. One such visualization is plotted in Fig. 9, which shows the stable manifold of saliva particle marked by the bended longitudinal jet in the flow direction. Upon reaching the vortex front and encountering the saddle point, saliva particles propagate along an orthogonal material line with a distinctive backward folding fractal-like pattern on a single (upper) limb (Fig. 9). With the introduction of new particles at each breathing cycle, saliva particles travel through the stable manifold until they reach the forefront vortical structure. At this point, they propagate along the unstable manifold rising through the upper limb of the vortex ring. Once they reach the vortex front’s saddle point, the particles are drawn away from it in the direction of the unstable manifold (blow-up region of the vortex front in Fig. 9). The vortex front near the end of its upper limb acts as a global roll-up pattern for the exhaled saliva particles.

V. CONCLUSION

We employed a coupled LES and Lagrangian particle tracking model to investigate saliva particle transport, the vortex dynamics, and LCS characteristics during normal human breathing through the nose and mouth. Our simulation incorporated the sharp interface curvilinear immersed boundary method to represent human anatomy. Saliva particle trajectories were tracked by Lagrangian particle tracking, with particle size ranging from 0.1 to 10 μm . Evaporation effects were addressed by reducing the particle size over time until reaching a diameter of 0.1 μm . The simulation was continued for about 91 s when the forefront of the saliva particle plume reached 2 m from the person passing the social distancing guideline of 6 ft.

Analyzing the simulation results of human breathing during the early stages of saliva plume formation, we found that breathing through nose can significantly influence the shape of the plume. Unaffected by the nose flow during the first breathing cycle at $t < 1$ s, saliva particles plume which exits the mouth behaves similar to the flow from the mouth only. Soon after, at $t = 1$ s, because of the flow from the nose, the mouth jet bends downward accumulating particles on the lower side of the shear layer. This is when the particle trajectory of the mouth and nose breathing starts to deviate from that of the mouth only breathing. Later at $t = 2.5$ s, when the first inhalation phase starts, the saliva plume forms the first vortex ring through the pinch-off process. As time goes by, more and more saliva particles merge with the forefront vortex, and because of the cross flow of the nose, the trailing jet bends downward and the topology of the primary vortex becomes asymmetrical.

Examining the simulation results of the normal breathing from the mouth and nose during the later stages, we observed that, as the

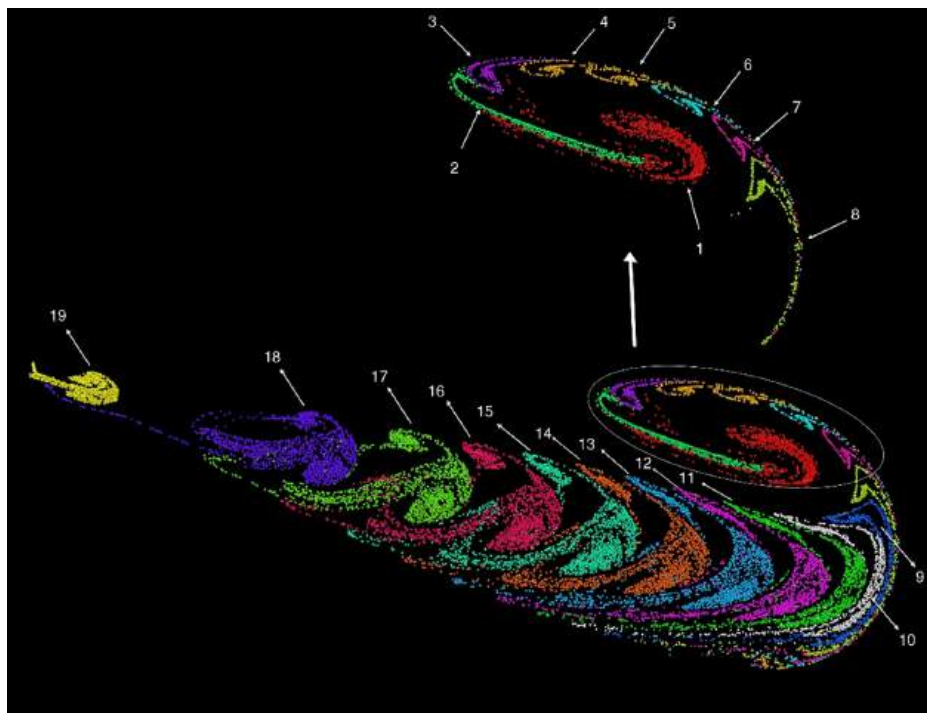


FIG. 9. Simulated trajectories of saliva particles at $t = 91.25$ s on a 5-cm-thick layer around the sagittal plane during normal breathing from nose and mouth simultaneously. It should be noted that this picture displays a thin slice (5-cm-thick layer) of the saliva particles in the longitudinal view. This thin layer of saliva particles is located in the middle of the flow domain—i.e., sagittal plane. This view allows to better visualize LCS that arise from the mouth and nose breathing. The exhaled particles generate periodic leading vortex rings marked with the numbers 1 through 19. The number indicates the sequence in which the vortex rings were generated. Saliva particles exhaled during each breathing cycle are tagged with a distinct color.

breathing process continues and with each new breathing cycle, particles in the plume gain momentum form small roll-up vortex rings and propagate forward along the jet flow of the mouth. The so-formed vortex rings move forward and eventually merge into the primary forefront vortex. Once they merged with the forefront vortex, these smaller vortex ring propagate upward outwards along the unstable manifold material line of the leading vortex. Throughout this process, the cross flow, which is induced by the flow from the nose openings, adds a downward momentum to the system and, consequently, tilts the stable manifold downward.

Finally, it should be noted that this study assumed that 75% of the tidal volume is exhaled through the mouth breathing, while 25% is related to the nose breathing. Therefore, the findings of this paper are limited to the above-mentioned ratio. This ratio was selected based on a preliminary study on a small group of people who mostly used their mouth for breathing. However, this ratio is more patient specific and, thus, could vary from person to person. In some cases, over 90% of the breathing occurs through nose, while in some other cases, most of the breathing is done via the mouth. To further investigate the dynamic of saliva transport at different nose and mouth breathing ratios, in a future study, we will numerically investigate normal human breathing with 90% and 10% through the nose and mouth, respectively.

ACKNOWLEDGMENTS

This study was supported by the Fulbright U.S. Scholar Program, which is sponsored by the U.S. Department of State and Fulbright España, and a grant from the U.S. Department of Energy's Office of Energy Efficiency and Renewable Energy (EERE) under the Water Power Technologies Office (WPTO) Award No. DE-EE0009450. Partial support was also provided by NSF (Grant No. 2233986). The contents of this article are solely the responsibility of the author and do not necessarily represent the official views of the Fulbright Program, the U.S. Department of Energy, or the Government of the United States, or the Fulbright España. The computational resources were provided by the Civil Engineering Department, and the Institute for Advanced Computational Sciences at Stony Brook University.

AUTHOR DECLARATIONS

Conflict of Interest

The authors have no conflicts to disclose.

Author Contributions

Hossein Seyedzadeh: Data curation (equal); Formal analysis (equal); Investigation (equal); Visualization (equal); Writing – original draft (equal); Writing – review & editing (equal). **Wayne Oaks:** Investigation (equal); Methodology (equal); Software (equal); Validation (equal); Writing – original draft (equal). **Jonathan Craig:** Investigation (equal); Writing – original draft (equal). **Mustafa Aksen:** Investigation (equal); Visualization (equal); Writing – original draft (equal). **Mario Sánchez Sans:** Investigation (equal); Writing – review & editing (equal). **Ali Khosronejad:** Conceptualization (lead); Data curation (equal); Formal analysis (equal); Funding acquisition (lead); Investigation (equal); Methodology (equal); Project administration (lead); Resources (lead); Software (lead); Supervision (lead); Validation (equal); Visualization (equal); Writing – original draft (equal); Writing – review & editing (equal).

DATA AVAILABILITY

The data that support the findings of this study are available from the corresponding author upon reasonable request.

APPENDIX: VALIDATION STUDY OF THE LAGRANGIAN MODEL

We validated the coupled EL approach using the experimental data measured in a stepped wind tunnel, reported in Refs. 65 and 66. The initial section of the wind tunnel, which is 4 cm high, 45.7 cm wide, and 5.2 m long, is followed by a 2.7 cm high step. The wind tunnel's cross section after the step is 6.7 cm high, 45.7 cm wide, and 1.4 m long. The bulk velocity of airflow in the wind tunnel is $U_0 = 9.39$ m/s and given the inlet height of 4 cm as the characteristic length, the flow has a Reynolds number of $\sim 2.5 \times 10^4$. Copper particles, with diameter of $d_p = 68.2 \mu\text{m}$ and density of $\rho_p = 8800$ kg/m³, are released into the wind tunnel and their propagation velocity is measured at a number of cross sections along the wind tunnel (see Refs. 65 and 66 for more details).

We replicated the experiments using a computational domain constructed by two structured background grid systems, which contained 1 m upstream and 1 m downstream of the step, of different resolution. The coarser grid system, denoted as grid A, consists of $\sim 325 \times 10^6$ computational grid nodes with a uniform grid

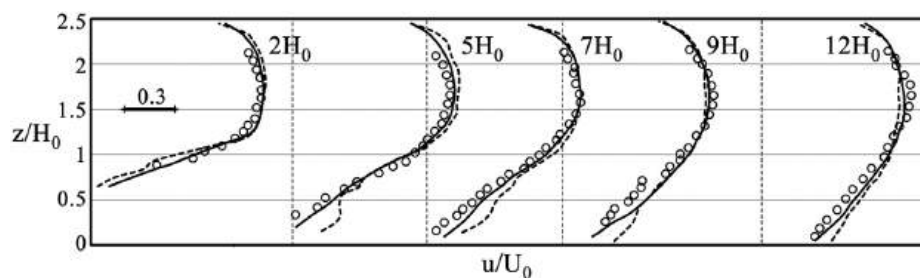


FIG. 10. Measured (circles) and computed (bold and dashed lines) results of the copper particle width-averaged streamwise velocity, u , normalized with the bulk velocity of $U_0 = 9.39$ m/s, at different cross sections downstream of the step in the wind tunnel. Dashed and bold lines mark the simulations results obtained from the computational grids A and B, respectively. The computed particle velocities represent the instantaneous values for many particles, while the measured values represent the mean velocity of many particles passing through each cross section. From left to right, the profiles represent the particle velocity at $2H_0$ to $12H_0$ from the step, where $H_0 = 2.7$ cm. z is the vertical coordinate.

resolution of 1.33 mm in all directions. The fine grid system, denoted as grid B, on the other hand, includes $\sim 442 \times 10^6$ grid nodes with a uniform resolution of ~ 1 mm in all directions. A temporal step of 0.1 ms was selected to achieve a Courant Friedrichs Lewy (CFL) number of 1.0 or smaller. The geometry of the wind tunnel's step and side walls were discretized with an unstructured triangular grid system. We ran precursor simulations using the periodic boundary condition along the streamwise direction to generate turbulent inflows. The precursor simulations provided inlet turbulent boundary conditions and were imposed at the inlet boundary of the simulations with grid A and B. For more details regarding the precursor LES methodology, the reader is referred to Refs. 67 and 68.

Using a one-way coupling approach, we carried out the Eulerian flow field simulation and Lagrangian particle tracking to obtain trajectories of 50 000 particles released at the inlet for about 0.07 s. In Fig. 10, the computed instantaneous width-averaged streamwise velocity of particle is compared with the corresponding measured values at five cross sections downstream of the step.

As seen in this figure, the computed results of the particle velocity with grid B are generally in a good agreement with the measured data. Overall, the simulation results on both grid systems at $z/H_0 > 0.75$ seem to be in a relatively good agreement with the measured data. The discrepancy between the measured and computed particle velocity starts to increase in the regions close to the bottom wall, $z/H_0 < 0.75$, where there are strong shear layer and secondary flows. A comparison between the simulation results on grid A and B clearly shows that the observed discrepancy could be associated with the resolution of the computational grid system in this region.

REFERENCES

- W. H. Organization, *WHO Coronavirus (COVID-19) Dashboard* (W. H. Organization, 2023).
- L. Bourouiba, "Turbulent gas clouds and respiratory pathogen emissions: Potential implications for reducing transmission of COVID-19," *Jama* **323**, 1837 (2020).
- A. Khosronejad, C. Santoni, K. Flora, Z. Zhang, S. Kang, S. Payabvash, and F. Sotiropoulos, "Fluid dynamics simulations show that facial masks can suppress the spread of COVID-19 in indoor environments," *AIP Adv.* **10**, 125109 (2020).
- R. Mittal, R. Ni, and J.-H. Seo, "The flow physics of COVID-19," *J. Fluid Mech.* **894**, F2 (2020).
- M. Rosti, S. Olivieri, M. Cavaioia, A. Seminara, and A. Mazzino, "Fluid dynamics of COVID-19 airborne infection suggests urgent data for a scientific design of social distancing," *Sci. Rep.* **10**, 22426 (2020).
- V. D'Alessandro, M. Falone, L. Giammichele, and R. Ricci, "Eulerian-Lagrangian modeling of cough droplets irradiated by ultraviolet-C light in relation to SARS-CoV-2 transmission," *Phys. Fluids* **33**, 031905 (2021).
- A. Fabregat, F. Gisbert, A. Vernet, S. Dutta, K. Mittal, and J. Pallarès, "Direct numerical simulation of the turbulent flow generated during a violent expiratory event," *Phys. Fluids* **33**, 035122 (2021).
- D. Fontes, J. Reyes, K. Ahmed, and M. Kinzel, "A study of fluid dynamics and human physiology factors driving droplet dispersion from a human sneeze," *Phys. Fluids* **32**, 111904 (2020).
- P. Katre, S. Banerjee, S. Balusamy, and K. C. Sahu, "Fluid dynamics of respiratory droplets in the context of COVID-19: Airborne and surfaceborne transmissions," *Phys. Fluids* **33**, 081302 (2021).
- H. Li, F. Y. Leong, G. Xu, C. W. Kang, K. H. Lim, B. H. Tan, and C. M. Loo, "Airborne dispersion of droplets during coughing: A physical model of viral transmission," *Sci. Rep.* **11**, 4617 (2021).
- G. Zeng, L. Chen, H. Yuan, A. Yamamoto, H. Chen, and S. Maruyama, "Analysis of airborne sputum droplets flow dynamic behaviors under different ambient conditions and aerosol size effects," *Chemosphere* **307**, 135708 (2022).
- G. Zeng, L. Chen, H. Yuan, A. Yamamoto, and S. Maruyama, "Evaporation flow characteristics of airborne sputum droplets with solid fraction: Effects of humidity field evolutions," *Phys. Fluids* **33**, 123308 (2021).
- D. S. Hui, B. K. Chow, L. Chu, S. S. Ng, N. Lee, T. Gin, and M. T. Chan, "Exhaled air dispersion during coughing with and without wearing a surgical or N95 mask," *PLoS One* **7**, e50845 (2012).
- T. Dbouk and D. Drikakis, "On respiratory droplets and face masks," *Phys. Fluids* **32**, 063303 (2020).
- M.-R. Pendar and J. C. Páscoa, "Numerical modeling of the distribution of virus carrying saliva droplets during sneeze and cough," *Phys. Fluids* **32**, 083305 (2020).
- A. Issakhov, Y. Zhandaulet, P. Omarova, A. Alimbek, A. Borsikbayeva, and A. Mustafayeva, "A numerical assessment of social distancing of preventing airborne transmission of COVID-19 during different breathing and coughing processes," *Sci. Rep.* **11**, 9412 (2021).
- Y. Liu, E. A. Matida, and M. R. Johnson, "Experimental measurements and computational modeling of aerosol deposition in the Carleton-civic standardized human nasal cavity," *J. Aerosol Sci.* **41**, 569 (2010).
- S. Majee, A. Saha, S. Chaudhuri, D. Chakravorty, and S. Basu, "Two-dimensional mathematical framework for evaporation dynamics of respiratory droplets," *Phys. Fluids* **33**, 103302 (2021).
- R. Mittal, C. Meneveau, and W. Wu, "A mathematical framework for estimating risk of airborne transmission of COVID-19 with application to face mask use and social distancing," *Phys. Fluids* **32**, 101903 (2020).
- M. Zhou and J. Zou, "A dynamical overview of droplets in the transmission of respiratory infectious diseases," *Phys. Fluids* **33**, 031301 (2021).
- W. F. Wells, "On air-borne infection. Study II. Droplets and droplet nuclei," *Am. J. Hyg.* **20**, 611 (1934).
- B. Stiehl, R. Shrestha, S. Schroeder, J. Delgado, A. Bazzi, J. Reyes, M. Kinzel, and K. Ahmed, "The effect of relative air humidity on the evaporation time-scales of a human sneeze," *AIP Adv.* **12**, 075210 (2022).
- E. Renzi and A. Clarke, "Life of a droplet: Buoyant vortex dynamics drives the fate of micro-particle expiratory ejecta," *Phys. Fluids* **32**, 123301 (2020).
- C. Lieber, S. Melekidis, R. Koch, and H.-J. Bauer, "Insights into the evaporation characteristics of saliva droplets and aerosols: Levitation experiments and numerical modeling," *J. Aerosol Sci.* **154**, 105760 (2021).
- A. Khosronejad, S. Kang, F. Wermelinger, P. Koumoutsakos, and F. Sotiropoulos, "A computational study of expiratory particle transport and vortex dynamics during breathing with and without face masks," *Phys. Fluids* **33**, 066605 (2021).
- M. S. Islam, M. Rahman, A. Arsalanloo, H. M. Beni, P. Larpruenrudee, N. S. Bennett, R. Collins, T. Gemci, M. Taylor, and Y. Gu, "How SARS-CoV-2 omicron droplets transport and deposit in realistic extrathoracic airways," *Phys. Fluids* **34**, 113320 (2022).
- S. Behera, B. Bhardwaj, and A. Agrawal, "Effect of co-flow on fluid dynamics of a cough jet with implications in spread of COVID-19," *Phys. Fluids* **33**, 101701 (2021).
- H. Salati, D. F. Fletcher, M. Khamooshi, J. Dong, K. Ito, S. Vahaji, and K. Inthavong, "Exhaled jet and viral-laden aerosol transport from nasal sneezing," *Aerosol Air Qual. Res.* **22**, 210338 (2022).
- S. Behera, B. A. Khan, and A. K. Saha, "Characterization of the turbulent field behavior of an elevated jet-in crossflow investigated using direct numerical simulation," *Phys. Fluids* **35**, 015157 (2023).
- X. Zhang, K. Wang, X. Wen, C. He, Y. Liu, and W. Zhou, "Experimental study of time-resolved simultaneous velocity and concentration fields of an inclined jet in crossflow," *Int. J. Heat Mass Transfer* **188**, 122622 (2022).
- K. Bradshaw, P. Warfield-McAlpine, S. Vahaji, J. Emmerling, H. Salati, R. Sacks, D. F. Fletcher, N. Singh, and K. Inthavong, "New insights into the breathing physiology from transient respiratory nasal simulation," *Phys. Fluids* **34**, 115103 (2022).
- W. R. Oaks, J. Craig, C. Duran, F. Sotiropoulos, and A. Khosronejad, "On the Lagrangian dynamics of saliva particles during normal mouth breathing," *Phys. Fluids* **34**, 041904 (2022).

- ³³G. Haller, "Distinguished material surfaces and coherent structures in three-dimensional fluid flows," *Physica D* **149**, 248 (2001).
- ³⁴M. Beneitez, Y. Duguet, P. Schlatter, and D. S. Henningson, "Edge manifold as a Lagrangian coherent structure in a high-dimensional state space," *Phys. Rev. Res.* **2**, 033258 (2020).
- ³⁵G. Haller, "Lagrangian coherent Structures," *Annu. Rev. Fluid Mech.* **47**, 137 (2015).
- ³⁶W. R. Oaks, S. Kang, X. Yang, and A. Khosronejad, "Lagrangian dynamics of contaminant particles released from a point source in New York City," *Phys. Fluids* **34**, 073303 (2022).
- ³⁷T. Peacock and G. Haller, "Lagrangian coherent structures: The hidden skeleton of fluid flows," *Phys. Today* **66**(2), 41 (2013).
- ³⁸G. Spedding, G. Jacobs, and M. Hemati, "Control of Lagrangian coherent structures at stagnation and separation locations on airfoils," Technical Report No. AFRL-AFOSR-VA-TR-2020-0074 (University of Southern California, 2019).
- ³⁹G. Haller, "Lagrangian coherent structures from approximate velocity data," *Phys. Fluids* **14**, 1851 (2002).
- ⁴⁰C. F. D. Control, *Guidance for Unvaccinated People* (C. F. D. Control, 2023).
- ⁴¹E. Y. Shiu, N. H. Leung, and B. J. Cowling, "Controversy around airborne versus droplet transmission of respiratory viruses: Implication for infection prevention," *Curr. Opin. Infect. Dis.* **32**, 372 (2019).
- ⁴²A. Khosronejad and F. Sotiropoulos, "Numerical simulation of sand waves in a turbulent open channel flow," *J. Fluid Mech.* **753**, 150 (2014).
- ⁴³A. Khosronejad and F. Sotiropoulos, "On the genesis and evolution of Barchan dunes: Morphodynamics," *J. Fluid Mech.* **815**, 117 (2017).
- ⁴⁴A. Khosronejad and F. Sotiropoulos, "A short note on the simulation of turbulent stratified flow and mobile bed interaction using the continuum coupled flow and morphodynamics model," *Environ. Fluid Mech.* **20**, 1511 (2020).
- ⁴⁵A. Calderer, X. Yang, D. Angelidis, A. Khosronejad, T. Le, S. Kang, A. Gilmanov, L. Ge, and I. Borazjani, *Virtual Flow Simulator* (University of Minnesota, 2015).
- ⁴⁶S. Chawdhary, A. Khosronejad, G. Christodoulou, and F. Sotiropoulos, "Large eddy simulation of density current on sloping beds," *Int. J. Heat Mass Transfer* **120**, 1374 (2018).
- ⁴⁷S. Kang, A. Lightbody, C. Hill, and F. Sotiropoulos, "High-resolution numerical simulation of turbulence in natural waterways," *Adv. Water Resour.* **34**, 98 (2011).
- ⁴⁸A. Khosronejad, C. Feist, J. Marr, and F. Sotiropoulos, "Experimental and computational study of a high-Reynolds jet flow," *Can. J. Civ. Eng.* **44**, 569 (2017).
- ⁴⁹A. Khosronejad, A. Hansen, J. Kozarek, K. Guentzel, M. Hondzo, M. Guala, P. Wilcock, J. Finlay, and F. Sotiropoulos, "Large eddy simulation of turbulence and solute transport in a forested headwater stream," *J. Geophys. Res.: Earth Surf.* **121**, 146, <https://doi.org/10.1002/2014JF003423> (2016).
- ⁵⁰A. Khosronejad, S. Kang, A. Farhadzadeh, and F. Sotiropoulos, "On the genesis and evolution of Barchan dunes: Hydrodynamics," *Phys. Fluids* **32**, 086602 (2020).
- ⁵¹A. Khosronejad, L. Mendelson, A. H. Techet, S. Kang, D. Angelidis, and F. Sotiropoulos, "Water exit dynamics of jumping archer fish: Integrating two-phase flow large-eddy simulation with experimental measurements," *Phys. Fluids* **32**, 011904 (2020).
- ⁵²F. Sotiropoulos and A. Khosronejad, "Sand waves in environmental flows: Insights gained by coupling large-eddy simulation with morphodynamics," *Phys. Fluids* **28**, 021301 (2016).
- ⁵³A. Khosronejad and F. Sotiropoulos, "Reply to comment by Sookhak Lari, K. and Davis, G. B. on 'Large eddy simulation of turbulence and solute transport in a forested headwater stream': Invalid representation of scalar transport by the act of diffusion," *J. Geophys. Res.: Earth Surf.* **123**, 1610, <https://doi.org/10.1029/2018JF004663> (2018).
- ⁵⁴S. Morsi and A. Alexander, "An investigation of particle trajectories in two-phase flow systems," *J. Fluid Mech.* **55**, 193 (1972).
- ⁵⁵H. Li, F. Y. Leong, G. Xu, Z. Ge, C. W. Kang, and K. H. Lim, "Dispersion of evaporating cough droplets in tropical outdoor environment," *Phys. Fluids* **32**, 113301 (2020).
- ⁵⁶World Health Organization (WHO), *Natural Ventilation for Infection Control in Health-Care Settings*, edited by J. Atkinson, Y. Chartier, C. L. Pessoa-Silva, P. Jensen, Y. Li, and W.-H. Seto (American Institute of Chemical Engineers, 2009), pp. 1-133.
- ⁵⁷M. Gharib, E. Rambod, and K. Shariff, "A universal time scale for vortex ring formation," *J. Fluid Mech.* **360**, 121 (1998).
- ⁵⁸K. Mahesh, "The interaction of jets with crossflow," *Annu. Rev. Fluid Mech.* **45**, 379 (2013).
- ⁵⁹A. R. Karagozian, "Transverse jets and their control," *Prog. Energy Combust. Sci.* **36**, 531 (2010).
- ⁶⁰R. M. Kelso, T. Lim, and A. Perry, "An experimental study of round jets in cross-flow," *J. Fluid Mech.* **306**, 111 (1996).
- ⁶¹L. Cortelezzi and A. R. Karagozian, "On the formation of the counter-rotating vortex pair in transverse jets," *J. Fluid Mech.* **446**, 347 (2001).
- ⁶²T. F. Fric and A. Roshko, "Vortical structure in the wake of a transverse jet," *J. Fluid Mech.* **279**, 1 (1994).
- ⁶³C. F. D. Control, *Guidance for Unvaccinated People* (C. F. D. Control, 2021).
- ⁶⁴P. Maremonti, "Existence and stability of time-periodic solutions to the Navier-Stokes equations in the whole space," *Nonlinearity* **4**, 503 (1991).
- ⁶⁵J. R. Fessler and J. K. Eaton, "Turbulence modification by particles in a backward-facing step flow," *J. Fluid Mech.* **394**, 97 (1999).
- ⁶⁶F. Greifzu, C. Kratzsch, T. Forgber, F. Lindner, and R. Schwarze, "Assessment of particle-tracking models for dispersed particle-laden flows implemented in OpenFOAM and ANSYS FLUENT," *Eng. Appl. Comput. Fluid Mech.* **10**, 30 (2016).
- ⁶⁷A. Khosronejad, K. Flora, and S. Kang, "Effect of inlet turbulent boundary conditions on scour predictions of coupled LES and morphodynamics in a field-scale river: Bankfull flow conditions," *J. Hydraul. Eng.* **146**, 04020020 (2020).
- ⁶⁸W. R. Oaks, K. Flora, and A. Khosronejad, "Eulerian numerical modeling of contaminant transport in Lower Manhattan, New York City, from a point-source release under the dominant wind condition: Insights gained via LES," *Atmos. Environ.* **262**, 118621 (2021).